Nonlinear Modeling of the Dynamic Effects of Arterial Pressure and CO_2 Variations on Cerebral Blood Flow in Healthy Humans

Georgios D. Mitsis*, *Member, IEEE*, Marc J. Poulin, Peter A. Robbins, and Vasilis Z. Marmarelis, *Fellow, IEEE*

***Abstract*—The effect of spontaneous beat-to-beat mean arterial blood pressure fluctuations and breath-to-breath end-tidal CO_2 fluctuations on beat-to-beat cerebral blood flow velocity variations is studied using the Laguerre–Volterra network methodology for multiple-input nonlinear systems. The observations made from experimental measurements from ten healthy human subjects reveal that, whereas pressure fluctuations explain most of the high-frequency blood flow velocity variations (above 0.04 Hz), end-tidal CO_2 fluctuations as well as nonlinear interactions between pressure and CO_2 have a considerable effect in the lower frequencies (below 0.04 Hz). They also indicate that cerebral autoregulation is strongly nonlinear and dynamic (frequency-dependent). Nonlinearities are mainly active in the low-frequency range (below 0.04 Hz) and are more prominent in the dynamics of the end-tidal CO_2-blood flow velocity relationship. Significant nonstationarities are also revealed by the obtained models, with greater variability evident for the effects of CO_2 on blood flow velocity dynamics.**

***Index Terms*—Cerebral autoregulation, cerebral hemodynamics, Laguerre–Volterra network, nonlinear modeling, nonstationary systems, Volterra kernels.**

I. Introduction

CEREBROVASCULAR resistance is controlled by multiple homeostatic mechanisms, which regulate cerebral blood flow (CBF). The cerebrovascular bed is able to maintain a relatively constant CBF despite changes in cerebral perfusion pressure [1]–[3]. Cerebral autoregulation was long viewed as a static phenomenon, whereby the "steady-state" pressure-flow relationship is described by a sigmoidal curve with a wide plateau, suggesting that CBF remains constant despite changes in pressure within certain bounds. However, with the development of transcranial Doppler (TCD) ultrasonography for the noninvasive measurement of CBF velocity (CBFV), which has been shown to represent CBF well in most practical cases, in the middle cerebral artery with high temporal resolution, it was found that CBFV can vary rapidly in response to variations of systemic arterial blood pressure (ABP) over various time scales [4], [5].

The availability of such data has revealed information about the dynamic properties of cerebral autoregulation and the quantitative manner in which rapid changes in pressure induce rapid changes in flow. It has also cast doubt on the validity of the notion of "steady-state," since no such "steady-state" is ever observed in the natural operation of cerebral circulation. In addition to controlled experiments, spontaneous fluctuations of beat-to-beat mean ABP (MABP) and mean CBFV (MCBFV) possess broadband characteristics and have been recently employed for the study of dynamic cerebral autoregulation, using linear [6]–[9] and nonlinear [10], [11] modeling methods. Impulse response or transfer function estimates in linear analysis and Volterra models in nonlinear analysis have demonstrated that cerebral autoregulation is more effective in the low-frequency range (below 0.1 Hz), where most of the MABP spectral power resides (i.e., most spontaneous MABP changes do not cause large MCBFV variations). The presence of significant nonlinearities, which are more prominent in this low-frequency range, was indicated in [11], suggesting that cerebral autoregulation mechanisms exhibit dynamic (i.e., frequency-dependent) nonlinearities.

It is also well established that arterial gases produce vascular responses in cerebral vessels [1]–[3]. Arterial CO_2 tension (P_{aCO_2}) is one of the strongest physiologic modulators of CBF [1]. The main mechanism of P_{aCO_2} reactivity is described by the pH hypothesis [12], which postulates that systemic CO_2 crosses the blood-brain barrier and modulates the extracellular and perivascular $[H^+]$, thus changing the smooth muscle properties. Specifically, hypercapnia induces vasodilation and hypocapnia causes vasoconstriction. According to the static point of view, hypercapnia narrows the autoregulatory plateau, making autoregulation less effective, while hypocapnia widens the plateau.

A number of studies have examined CBFV responses to step changes in CO_2 tension [13]–[16], and it was shown that this response is not instantaneous but lags the CO_2 tension changes by several seconds. Poulin *et al.* developed a simple one-compartmental model for the cerebrovascular response to hypercapnia [15], characterized by a time constant, a gain term and a pure delay. A second compartment with a larger time constant (on the order of 7 min) had to be included for the hypocapnic response [16], since a secondary, slow adaptation (increase) of CBFV to the hypocapnic stimulus was reported. An asymmetry in the

Manuscript received April 8, 2003; revised March 31, 2004. This work was supported by grant no. P41-EB001978 awarded to the Biomedical Simulations Resource at the University of Southern California by the National Institutes of Health and by the Wellcome Trust, UK. *Asterisk indicates corresponding author*.

*G. D. Mitsis is with the Department of Biomedical Engineering, University of Southern California, OHE 500, University Park, Los Angeles, CA 90089 USA (e-mail: gmitsis@bmsr.usc.edu).

M. J. Poulin was with the University Laboratory of Physiology, University of Oxford, Oxford OX1 3PT, U.K.. He is now with the Department of Physiology and Biophysics, Faculty of Medicine, University of Calgary, HMRB-212, Calgary, AB T2N 4N1, Canada (e-mail: poulin@ucalgary.ca).

P. A. Robbins is with the University Laboratory of Physiology, University of Oxford, Oxford OX1 3PT, U.K. (e-mail: peter.robbins@physiol.ox.ac.uk).

V. Z. Marmarelis is with the Department of Biomedical Engineering, University of Southern California, OHE 500, University Park, Los Angeles, CA 90089 USA (e-mail: vzm@bmsr.usc.edu).

Digital Object Identifier 10.1109/TBME.2004.834272

on-transient and off-transient responses to hypocapnia was also reported, the on-transient being significantly faster and with a smaller gain than the off-transient, and a pure time delay equal to 3.9 s was estimated [16]. Nonlinear mathematical models were developed in [17], [18] in order to describe the interactions between autoregulation, CO_2 reactivity and intracranial pressure, whereby the interaction between P_{aCO_2} and autoregulation was modeled with a sigmoidal relationship.

Since P_{aCO_2} reactivity can be assessed by breath-to-breath end-tidal $CO_2(P_{ETCO_2})$ measurements, spontaneous P_{ETCO_2} variations may be employed to study the dynamic characteristics of the P_{aCO_2}-MCBF relationship, in a similar manner to spontaneous MABP variations. To our knowledge, this has been done in only one study so far [19], in which Panerai *et al.* employed causal finite-impulse response filters and spontaneous breath-to-breath P_{ETCO_2} variations to assess the effect of arterial CO_2 on MCBFV. It was found that when used along with beat-to-beat MABP variations, P_{ETCO_2} variations improve the error performance of the model considerably (though pressure fluctuations explain a larger fraction of CBFV variability). The temporal characteristics of the MABP-MCBFV and P_{ETCO_2}-MCBFV relations were obtained in the form of impulse responses. The possibility of interactions between the two input variables was also investigated, but there were no significant interactions reported.

However, in the aforementioned study, the dependence of MCBFV on the two input variables (MABP and P_{ETCO_2}) was assumed to be linear and nonlinearities were included in the form of second-order cross-terms only. Cerebral autoregulation is nevertheless characterized by inherent and significant nonlinearities [10], [11] and in order to obtain accurate models, these nonlinearities should not be neglected. The Laguerre–Volterra network (LVN) methodology [20] was employed successfully to model the MABP-MCBFV nonlinear dynamic relationship in [11]. Here, we employ a different formulation of the LVN, termed the multiple-input LVN (MI-LVN), suitable for modeling nonlinear systems with multiple inputs in order to assess the nonlinear dynamic effects of MABP and P_{ETCO_2} on MCBFV as well as the effects of their nonlinear interactions.

II. Methods

A. Experimental Methods

Ten subjects participated in the study (age 30.4 ± 20.1 years, height 179.6 ± 8.9 cm, weight 76.6 ± 14.0 Kg). None of the participants was on any medication and all of them were normotensive and did not have a history of any cardiovascular, pulmonary or cerebrovascular diseases. The study was approved by the Central Oxford Research Ethics Committee and the procedures were explained to all the participants, who gave their written consent before the study. The subjects were refrained from food and caffeine-containing beverages for at least 4 hr before the sessions, which lasted about 40 min. Each subject's resting P_{ETCO_2} was measured with a nasal catheter.

According to the experimental protocol, the mean value of end-tidal $P_{O_2}(P_{ETO_2})$ was held at 100 torr, whereas the mean value of P_{ETCO_2} was held at about 1.5 torr above the subject's normal value (as determined on that day). Respiratory volumes were measured with a turbine volume transducer (SensorMedics VWM Series, CardioKinetics, Salford, U.K.). Gas was sampled continuously at a rate of 20ml/min and its composition (fractional concentrations of O_2, CO_2, and N_2) was measured by a mass spectrometer (model MGA3000, Airspec, Biggin Hill, U.K.). The experimental variables were sampled every 20 ms. Accurate control of the respiratory gases was achieved by using the dynamic end-tidal forcing technique [21], [22], whereby a controlling computer maintains the end-tidal values close to their desired level by receiving feedback on a breath-to-breath basis and by using a fast gas-mixing system. It has been suggested [23], [24] that P_{ETCO_2} changes are a good index of P_{aCO_2} changes in both old and young subjects at rest.

ABP was monitored continuously in the finger by photoplethysmography (Ohmeda 2300, Finapres). The pressure data were sampled every 10 ms. The reliability of this technique for measuring ABP has been established in previous studies [25], [26]. The Doppler signals were measured with a 2-MHz Doppler ultrasound system (PCDop 842, SciMed, Bristol, U.K.) in the right middle cerebral artery (MCA). The maximum and intensity weighted Doppler shifts were made available as analog signals and were updated every 10 ms (at which intervals a new spectrum was calculated). The signals were sampled every 10 ms (DAQWare, National Instruments United Kingdom, Newbury, U.K.) and were saved, along with the time occurrence of each QRS complex and the pressure data for the subsequent analysis. The MCA was identified by an insonation pathway through the right temporal window just above the zygomatic arch by using search techniques described in [27] and [28]. Optimization of the signals was performed by varying the sample volume depth incrementally and the angle of insonance at each depth, in order to obtain the best quality Doppler shifts corresponding to the maximum power signal. In order to maintain the optimal insonation position and angle, the Doppler probe was securely positioned in a headband device (Muller and Moll Fixation, Nicolet Instruments).

Measurements of the velocity corresponding to the maximum Doppler shift V_P, which is associated with the fastest moving blood in the vessel, the intensity-weighted mean velocity V_{IWM}, which corresponds to the mean velocity of the blood averaged over the entire cross section and is based on the entire velocity spectrum and the reflected Doppler signal power P, which is an index of the cross-section area were collected every 10 ms. Mean values for each signal ($\overline{V}_P$, $\overline{V}_{IWM}$, $\overline{P}$, and $\overline{P \cdot V}_{IWM}$) were calculated over each cardiac cycle. The variables $\overline{V}_P$, $\overline{V}_{IWM}$, and $\overline{P \cdot V}_{IWM}$ can be all used to represent blood flow, although $\overline{V}_P$ is the easiest to measure and has been used extensively in the literature as a surrogate variable for CBF [5]–[11], [15], [16], [19]. $\overline{V}_P$ does not account for any changes in vessel size, and neither it nor $\overline{V}_{IWM}$ can be considered to be proportional to blood flow when major vessel size changes occur. However, it has been found [28] that changes occurring in the MCA cross-sectional area under control, hypoxic or hypercapnic conditions are minimal and that the temporal patterns of $\overline{V}_P$, $\overline{V}_{IWM}$ and $\overline{P \cdot V}_{IWM}$, as well as their average values, are very similar (as assessed by statistical analysis); therefore, beat-to-beat changes of all three reflect CBF changes well. A significant increase in MCA size (3.8% increase in Doppler power signal) was reported only under combined hypoxia and hypercapnia, whereby $\overline{V}_P$, $\overline{V}_{IWM}$ underestimated the changes in $\overline{P \cdot V}_{IWM}$ [28]. Since the mean values of P_{ETCO_2} and P_{ETO_2} were set at normal levels and spontaneous fluctuations around those values are employed in our case, $\overline{V}_P$ is employed as an index of CBF.

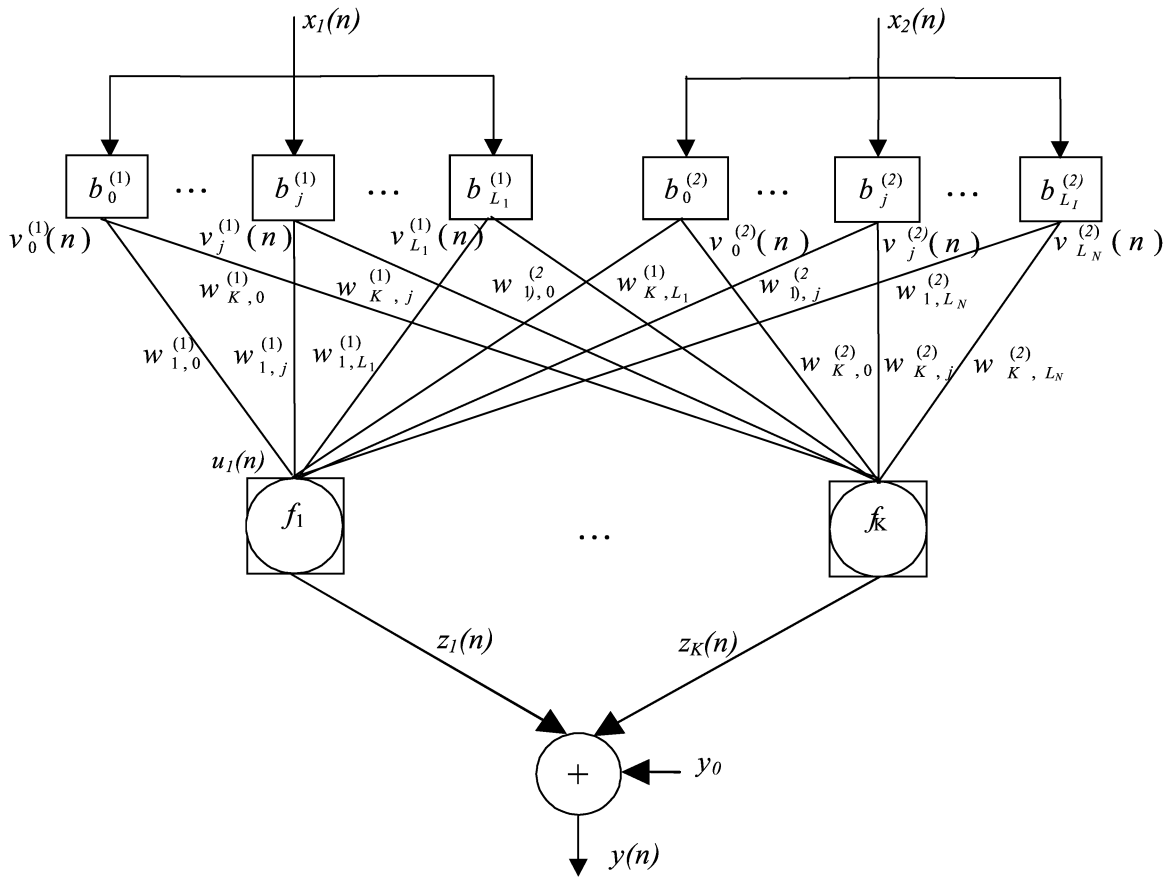

Fig. 1. The multiple-input Laguerre–Volterra network (MI-LVN) for a system with two inputs. The two Laguerre filter-banks $\left\{b_j^{(1)}\right\}$ and $\left\{b_j^{(2)}\right\}$ preprocess the inputs $x_1(n)$ and $x_2(n)$, respectively. The hidden units in the second layer receive a summation of the outputs from all Laguerre filters $\left\{v_j^{(i)}(n)\right\}$, weighted by $\left\{w_{k,j}^{(i)}\right\}$, as their input (i.e., $u_k(n) = \sum_{i=1}^{2}\sum_{j=0}^{L_i} w_{k,j}^{(i)} v_j^{(i)}(n)$) and have polynomial activation functions $\{f_k\}$, their output given by $z_k(n) = f_k[u_k(n)] = \sum_{m=1}^{Q} c_{m,k} u_k^m(n)$: The output $y(n)$ is formed by a nonweighted summation of the outputs of the hidden units $\{z_k\}$ and the output offset $y_0(y(n) = \sum_{k=1}^{K} z(n) + y_0)$.

Real time beat-to-beat mean values of ABP and CBFV were calculated by integrating the waveform of the sampled signals within each cardiac cycle (R-R interval). The beat-to-beat values were then interpolated and resampled at 1 Hz (after anti-aliasing low-pass filtering) to obtain equally spaced time series of MABP and MCBFV data. The breath-to-breath $P_{\mathrm{ETCO_2}}$ data were interpolated in order to obtain values every 1 s. Since practically all $P_{\mathrm{ETCO_2}}$ power lies below 0.1 Hz, there were no high-frequency artifacts inserted because of the interpolation.

B. Mathematical Methods

The LVN methodology is a variant of the general Volterra-Wiener approach [29], [30] and has been shown to yield accurate nonlinear methods from short stimulus-response records [20]. In this study, its extension for multiple-input systems is employed [31]. The equivalent LVN model of a two-input, Qth-order nonlinear system is shown in Fig. 1.

Each of the two inputs $x_1(n), x_2(n)$ is preprocessed by (i.e., convolved with) a different Laguerre filter-bank and the filter outputs are fully connected to a layer of hidden units with polynomial activation functions. The free parameters of the network of Fig. 1 are the Laguerre parameters (α_1, α_2) of the two filter-banks $\left\{b_j^{(1)}\right\}$ and $\left\{b_j^{(2)}\right\}$, the connection weights $\left\{w_{k,j}^{(i)}\right\}$, the polynomial coefficients $\{c_{m,k}\}$ and the output offset y_0. The total number of the MI-LVN parameters is equal to $(L_1 + L_2 + 2 + Q) \cdot K + 3$, where (L_1, L_2) are the maximum orders of the Laguerre functions employed in the two filter-banks, Q is the order of the polynomial activation functions and K is the number of hidden units. Note that this number of free parameters is linear with respect to Q, which ensures compact representations even for higher order systems.

The input–output data are used to train the network via an iterative gradient descent scheme. This is done through the following relations:

$$w_{k,j}^{(i),(r+1)} = w_{k,j}^{(i),(r)} + \gamma_w \left[\varepsilon^{(n)} f_k'(u_k(n)) v_j^{(i)}(n)\right]_r \quad (1)$$

$$c_{m,k}^{(r+1)} = c_{m,k}^{(r)} + \gamma_c \left[\varepsilon(n) u_k^m(n)\right]_r \quad (2)$$

$$y_0^{(r+1)} = y_0^{(r)} + \gamma_y \left[\varepsilon(n)\right]_r \quad (3)$$

$$\alpha_i^{(r+1)} = \alpha_i^{(r)} + \gamma_i \sum_{k=1}^{K}\sum_{m=1}^{Q}\sum_{j=0}^{L_i} m \times \left[\varepsilon(n) c_{m,k} w_{k,j}^{(i)} u_k^{m-1}(n) \frac{\partial v_j^{(i)}(n)}{\partial \alpha_i}\right]_r \quad i = 1, 2 \quad (4)$$

where the network variables and parameters are defined in Fig. 1, $\varepsilon(n)$ is the output prediction error, f_k' denotes the derivative of f_k with respect to u_k (i.e., $[f_k'(u_k(n))]_r = \sum_{q=1}^{Q} m \left[c_{q,k}(u_k^{(r)}(n))^{q-1}\right]_r$), r denotes the iteration index and $\gamma_w, \gamma_c, \gamma_y, \gamma_i$ are fixed positive learning constants. Note that the variables $v_j^{(i)}(n)$, $u_k(n)$, $f_k'(n)$ and $\varepsilon(n)$ are evaluated at the rth iteration for the current network parameter values, as denoted by $[\cdot]_r$ in (1)–(4).

With the use of two Laguerre filter-banks characterized by distinct Laguerre parameters (α_1, α_2) we can model the linear and nonlinear dynamics associated with each input as well as their nonlinear interactions. The MI-LVN representation of a system is equivalent to the general Volterra model, given below for a two-input, Qth-order system

$$y(n) = k_0 + \sum_{n=1}^{Q} \sum_{i_1=1}^{2} \cdots \sum_{i_2=1}^{2} \left\{ \sum_{m_1} \cdots \sum_{m_n} k_{i_1 \cdots i_n}(m_1, \ldots, m_n) \times x_{i_1}(n-m_1) \cdots x_{i_n}(n-m_n) \right\} \quad (5)$$

where $x_i(n)$ are the two system inputs, $y(n)$ is the system output and $k_{i_1 \ldots i_n}$ denotes the nth-order Volterra kernel of the system describing the nth-order nonlinear interactions between the two inputs. If $i_1 = \cdots = i_n = i$, $k_{i \ldots i}$ denotes the nth-order self-kernel corresponding to the ith input of the system, and describes the linear $(n = 1)$ and nonlinear $(n > 1)$ effects of the ith input on the output, whereas if some of $i_1 \cdots i_n$ are different, $k_{i_1 \ldots i_n}$ denotes the nth-order cross-kernel of the system, which describes the nonlinear interactions between the two inputs. The Volterra kernels in (5) can be expressed in terms of the trained network parameters as follows:

$$k_0 = y_0 \quad (6)$$

$$k_i(m) = \sum_{k=1}^{K} c_{1,k} \sum_{j=0}^{L_i} w_{k,j}^{(i)} b_j^{(i)}(m) \quad (7)$$

$$k_{ii}(m_1, m_2) = \sum_{k=1}^{K} c_{2,k} \sum_{j_1=0}^{L_i} \sum_{j_2=0}^{L_i} w_{k,j_1}^{(i)} \times w_{k,j_2}^{(i)} b_{j_1}^{(i)}(m_1) b_{j_2}^{(i)}(m_2) \quad (8)$$

$$k_{12}(m_1, m_2) = \sum_{k=1}^{K} c_{2,k} \sum_{j_1=0}^{L_1} \sum_{j_2=0}^{L_2} w_{k,j_1}^{(1)} \times w_{k,j_2}^{(2)} b_{j_1}^{(1)}(m_1) b_{j_2}^{(2)}(m_2) \quad (9)$$

$$, \ldots,$$

$$k_{i_1 \ldots i_n}(m_1, \ldots, m_n) = \sum_{k=1}^{K} c_{n,k} \sum_{j_1=0}^{L_{i_1}} \cdots \sum_{j_n=0}^{L_{i_n}} w_{k,j_1}^{(i_1)} \cdots w_{k,j_n}^{(i_n)} \times b_{j_1}^{(i_1)}(m_1) \cdots b_{j_n}^{(i_n)}(m_n). \quad (10)$$

The input signals of the MI-LVN model are the spontaneous MABP and P_{ETCO_2} fluctuations, while the output signal is the MCBFV variations (represented by $\overline{V}_P$). Six-minute data segments (i.e., with a length of 360 points) are used to train the network, after high-pass filtering (at 0.005 Hz) to remove very slow trends and normalizing to unit variance in order to avoid numerical problems related to the difference in the power of the signals.

The structural parameters of the MI-LVN are selected by applying the "minimum description length" (MDL) criterion [32] to the normalized mean-square error (NMSE) of the output prediction achieved by the model for the training data. The output prediction NMSE is defined as the sum of squares of the residuals of the model prediction (i.e., difference from the true output) over the sum of squares of the true output. This ensures that we obtain an accurate model representation of the system and avoid overfitting to the specific data segment. Following this procedure, a two-input MI-LVN with $L_1 = L_2 = 7$, $K = 3$, and $Q = 3$ is selected in all cases. Note that the total number of unknown parameters in this MI-LVN model is 60, which is extremely low compared to conventional techniques such as the cross-correlation technique, which would require the estimation of over 15 000 values for the first-, second-, and third-order kernels for a kernel memory of 100 lags. The achieved model parsimony results also in a significant improvement in the prediction NMSE. In order to avoid overtraining the network, a 2-min forward segment of data (adjacent to the 6-min training data segment) is used for cross-validation purposes. The network training is terminated when the prediction NMSE for the cross-validation segment is minimized.

TABLE I
MEAN VALUES (± STANDARD DEVIATIONS) OF MABP, P_{ETCO_2} AND MCBFV, AVERAGED OVER THE 40-MIN RECORDINGS FROM 10 SUBJECTS

MABP [mm Hg]	P_{ETCO_2} [mm Hg]	MCBFV[cm/sec]
77.2 ± 9.1	40.0 ± 1.9	59.1 ± 12.3

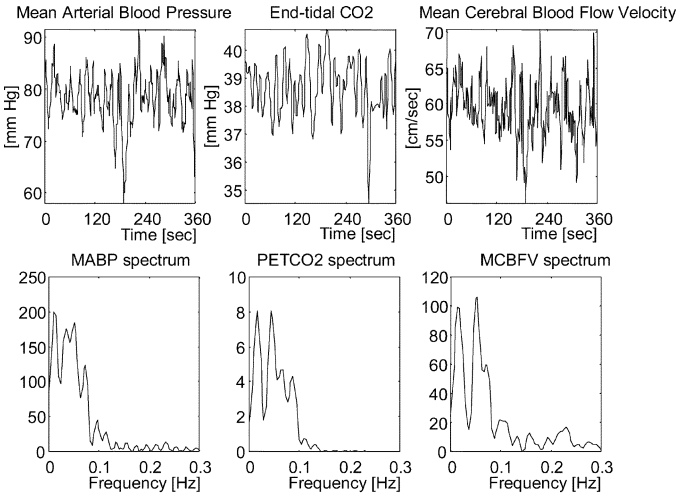

Fig. 2. Typical data segments used for model estimation. Top: time series, bottom: spectra of high-passed (at 0.005 Hz) signals.

III. RESULTS

The mean values of the MABP, P_{ETCO_2} and MCBFV data, averaged over the 40-min recordings for the ten subjects, are given in Table I. Typical 6-min data segments are shown in Fig. 2, along with the spectra of the corresponding high-passed data sets. Most of the MABP and MCBFV power resides below 0.1 Hz, however the latter exhibits some power up to 0.3 Hz. Almost all of the P_{ETCO_2} power lies below 0.1 Hz and is significantly smaller than that of the other two signals. To alleviate this, all signals are normalized so that they have unit variance prior to model estimation, as mentioned before.

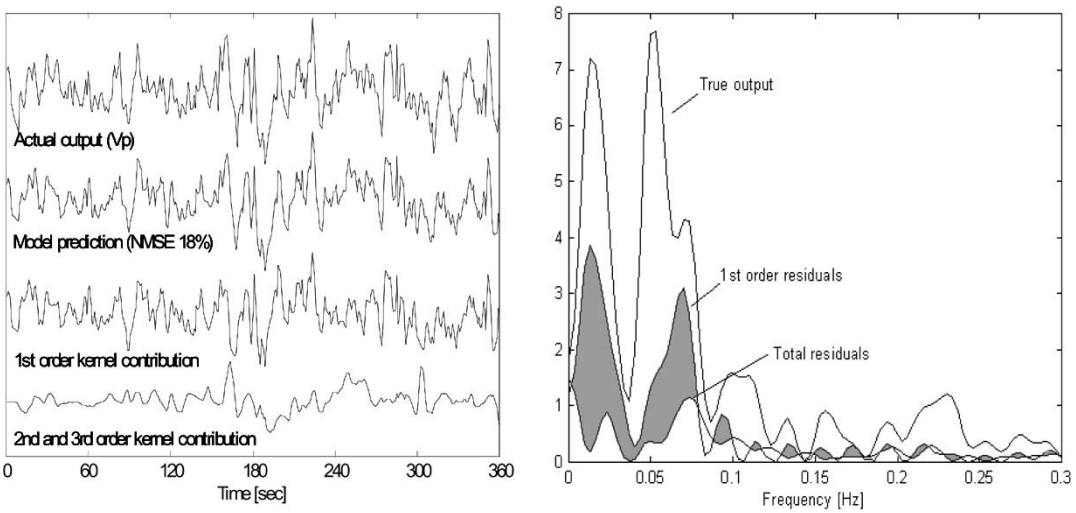

Fig. 3. Left: Actual CBFV output and model predictions (total, linear and nonlinear terms) for a typical data segment (taken from subject 091). Right: Spectra of actual output and model residuals (linear and total). The shaded area denotes the effect of the nonlinear terms in the frequency domain.

TABLE II
MEAN PREDICTION NMSES (± STANDARD DEVIATIONS) FOR ONE-INPUT AND TWO-INPUT MI-LVN MODELS

Model order	Model inputs		
	MABP	P_{ETCO_2}	MABP & P_{ETCO_2}
1	42.2 ± 7.2%	93.2 ± 2.7%	38.2 ± 6.5%
2	25.7 ± 8.3%	78.2 ± 6.4%	22.0 ± 6.0%
3	26.8 ± 7.6%	71.7 ± 4.8%	20.2 ± 5.4%

The average achieved in-sample prediction NMSE's are given in Table II for one input (MABP or P_{ETCO_2}) and two-input (MABP and P_{ETCO_2}) linear and nonlinear MI-LVN models. The complexity of the one-input and two-input models, in terms of the total number of their free parameters, is the same. While MABP fluctuations explain most of the MCBFV variations, as reported previously [19], the incorporation of P_{ETCO_2} fluctuations in the model reduces the achieved output prediction NMSEs (about 6% reduction in prediction NMSE). A significant reduction in the prediction NMSE, which satisfies the MDL criterion, is observed when nonlinear models are used instead of linear models (about 16% for one-input models and 18% for two-input models). The prediction NMSE achieved by third-order models is smaller than that achieved by second-order models in the two-input case and satisfies the MDL criterion; hence, a third-order model is selected.

The prediction achieved by the MI-LVN model for a typical data segment (taken from subject # 091) is shown in Fig. 3 (left), along with the contributions of the linear and nonlinear self and cross-terms. The model prediction is very close to the true output, as denoted by the low value of the NMSE (18%), and the contribution of the nonlinear terms is significant (reduction in the prediction NMSE is over 20%) and occurs mainly in the low frequencies. This is illustrated in Fig. 3 (right), where the spectrum of the true output is compared with the spectra of the total and first-order model residuals. The shaded area corresponds to the improvement achieved by the nonlinear terms and demonstrates that nonlinearities are prominent below 0.08 Hz, agreeing with the results presented in [11].

The contribution of each of the two model inputs as well as their nonlinear interactions can be seen in Fig. 4 (left) for the same segment. The top trace corresponds to the total model prediction, the second trace corresponds to the contribution of the MABP terms (linear and nonlinear terms), the third trace corresponds to the contribution of the P_{ETCO_2} terms and the bottom trace corresponds to the nonlinear (second and third-order) cross-terms. The MABP component accounts for 60% of the total model prediction power, the P_{ETCO_2} component accounts for an additional 17% of the total model prediction power, and the cross-term component accounts for the remaining 23%. The significance of the cross-term contribution is consistently observed among different data segments and contradicts the findings of previous studies [19], where it was found to be negligible. This is shown in Table III, where the achieved prediction NMSE of the third-order models after removing the model cross-terms is given, along with the total achieved NMSE and the reduction due to the cross-terms, averaged over all subjects. The average reduction is over 25% and exhibits considerable variability (from as low as 5% to as high as 70%, following roughly a χ^2 distribution). It is interesting to note here that in the one subject (# 147) that was considerably older than the other subjects (age: 82 yr) the average reduction due to the cross-terms was found to be substantially larger (average value of 47%). The spectra of the MABP and total residuals are shown in Fig. 4 (right) along with the true output spectrum. It is observed that most of the contribution of the MABP terms lies above 0.04 Hz, i.e., in the intermediate and high-frequency ranges, whereas the contribution of P_{ETCO_2} terms and the MABP-P_{ETCO_2} cross-terms lies below 0.08 Hz and is more prominent below 0.04 Hz, i.e., in the low-frequency range, as denoted by the shaded area.

By comparing Figs. 3 and 4, it can be inferred that the relative nonlinear-to-linear effect of MABP is greater for P_{ETCO_2} than MABP. This is illustrated in Fig. 5, where the contribution of each input (MABP and P_{ETCO_2}) in the total model prediction is decomposed into its linear and nonlinear (self) components for the same data segment. For this specific segment, the power of the linear MABP component corresponds to around 80% of the total MABP term power, whereas the power of the linear

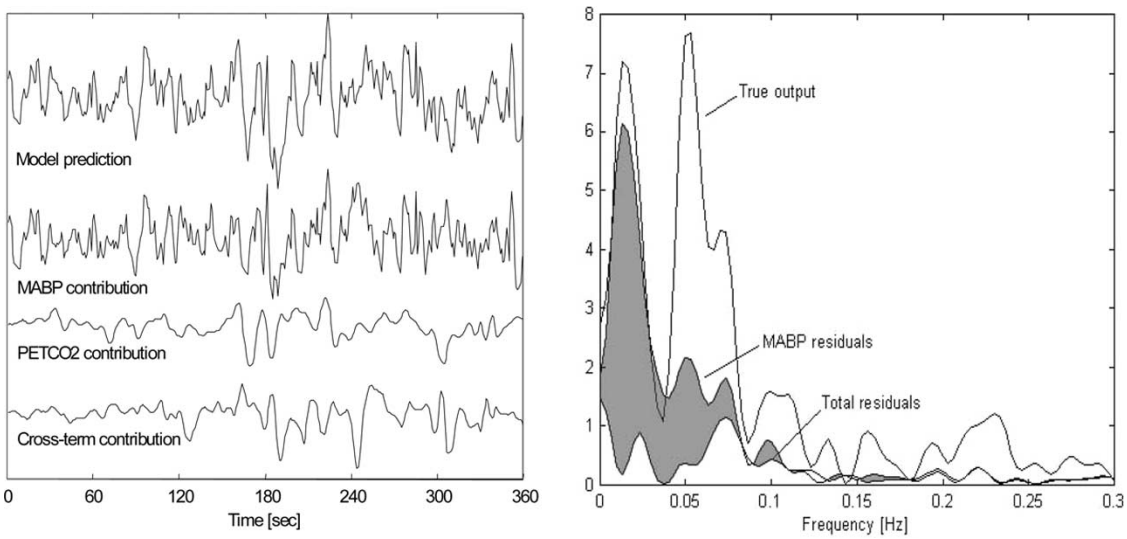

Fig. 4. Left: Actual output, LVN model prediction and contributions of MABP, P_{ETCO_2} and nonlinear interaction terms for the data segment of Fig. 3. Right: Spectra of output, MABP and total residuals. The shaded area shows the effect of the P_{ETCO_2} terms and cross-terms in the frequency domain.

TABLE III
MEAN PREDICTION NMSES (± STANDARD DEVIATIONS) FOR THIRD-ORDER MI-LVN MODELS WITH AND WITHOUT INCLUSION OF NONLINEAR TERMS AND CROSS-TERMS, CALCULATED OVER ALL TEN SUBJECTS

Prediction NMSE			NMSE reduction	
No cross-terms	No nonlinear terms	Total	Cross-terms	Nonlinear terms
49.8 ± 18.6%	52.2 ± 21.5%	20.2 ± 5.4%	27.1 ± 12.3%	31.2 ± 19.1%

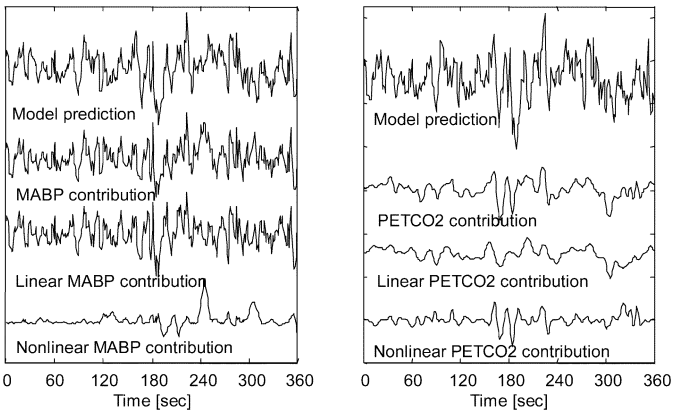

Fig. 5. Decomposition of the contribution of MABP (left) and P_{ETCO_2} terms (right) into linear and nonlinear components for the data segment of Fig. 3.

P_{ETCO_2} component is approximately equal to that of its nonlinear counterpart. The aforementioned observations are consistent among different segments and/or subjects, as shown in Table IV, where the power ratio of nonlinear to linear output components for MABP and P_{ETCO_2}, averaged over all subjects, is given. This ratio is smaller for MABP (the power of the nonlinear MABP component is equal to approximately 30% of its linear counterpart), while for P_{ETCO_2} the output component due to the nonlinear self-terms exhibits more power on the average than the linear component (ratio of around 1.2 or 120%), in agreement with the observations made from the typical data segment of Fig. 5. Considerable variability is observed in the contribution of the nonlinear terms to the output prediction NMSE. The average NMSE reduction due to the nonlinear model terms (self-terms for MABP, P_{ETCO_2} as well as cross-terms), in the case of third-order models, is also given in Table III. Its average value is over 31% and, as in the case of cross-terms only, it exhibits a wide range of values (from 5% to over 80%). The NMSE reduction is once more larger for the older subject $(63.1\% \pm 25.7\%)$. This is to be expected, since the cross-terms are part of the nonlinear terms, however it should be noted that the effects of the nonlinear self-terms and cross-terms on the model NMSE reduction are not additive (lack of orthogonality). The variability in the contribution of the nonlinear terms is reflected also in the form of the nonlinear self and cross-kernels.

TABLE IV
MEAN POWER RATIO (± STANDARD DEVIATIONS) OF NONLINEAR TO LINEAR MABP AND P_{ETCO_2} OUTPUT COMPONENTS OVER ALL SUBJECTS

	MABP	P_{ETCO_2}
Power ratio	0.31 ± 0.13	1.18 ± 0.45

The first-order MABP Volterra kernel, averaged over all ten, 40-min recordings (6-min sliding data segments with a 5-min overlap), is shown in Fig. 6 both in the time and frequency domains (log-linear plots, whereby the time lag values are incremented by one). The form of the kernel is very consistent among different segments and subjects, as demonstrated by the tight standard deviation bounds. The high-pass characteristic of the linear frequency response, after taking into account that MABP changes are translated into MCBFV changes in a mostly linear manner, implies that slow MABP changes are attenuated more effectively, i.e., autoregulation of pressure variations is more effective in the low-frequency range $(< 0.04$ Hz). A resonant peak is evident at around 0.2 Hz, with shoulders ap-

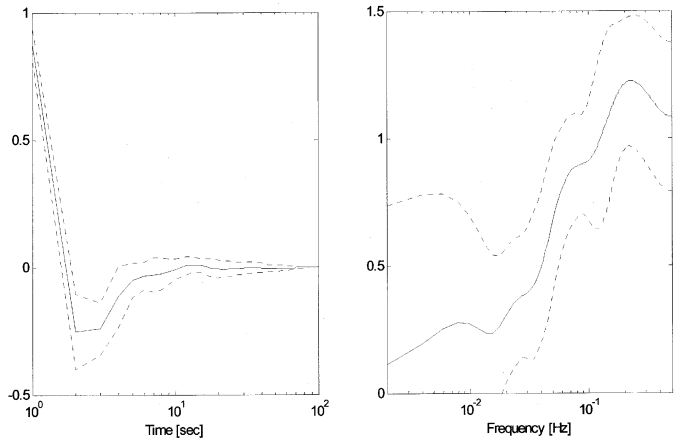

Fig. 6. The average first-order MABP kernel (solid line) and corresponding standard deviation (dotted lines), computed over the 40-min recordings from all ten subjects. Left: time domain, right: FFT magnitude.

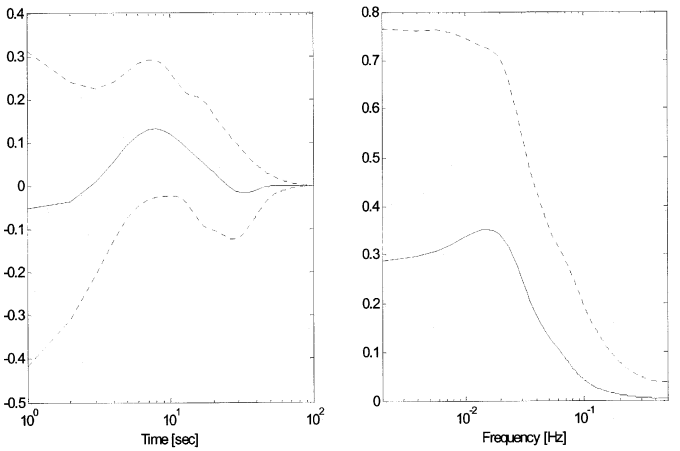

Fig. 7. The average first-order $P_{\mathrm{ETCO_2}}$ kernel (solid line) and corresponding standard deviation (dotted lines), computed over the 40-min recordings from all ten subjects. Left: time domain, right: FFT magnitude.

pearing at 0.025 and 0.07 Hz. Compared to the linear frequency response obtained when only MABP is used as an input [11], the MABP-MCBFV linear frequency response of Fig. 6 exhibits reduced gain in the low-frequency range, reflecting the fact that most of the low-frequency MCBFV variations are explained by $P_{\mathrm{ETCO_2}}$ fluctuations. In the intermediate and high-frequency ranges, the MABP first-order kernels are not affected by the inclusion of $P_{\mathrm{ETCO_2}}$ as an additional input variable.

The average first-order $P_{\mathrm{ETCO_2}}$ kernel over all recordings is shown in Fig. 7. It should be noted that the results shown here are obtained after shifting the $P_{\mathrm{ETCO_2}}$ data by 4 points (i.e., 4 s), since it was initially determined that a pure delay on the order of 3–4 s is present in the $P_{\mathrm{ETCO_2}}$ dynamics, in agreement with [16]. This delay appears in the form of high variance values for the initial time lags of the first- and second-order kernel estimates. When the analysis is repeated with the $P_{\mathrm{ETCO_2}}$ data shifted accordingly, the obtained kernels exhibit considerably reduced variance in their initial time lags and are not affected otherwise, while the prediction NMSEs remain roughly the same. The first-order $P_{\mathrm{ETCO_2}}$ frequency response (right) has most of its power below 0.015 Hz (notice the plateau)—giving

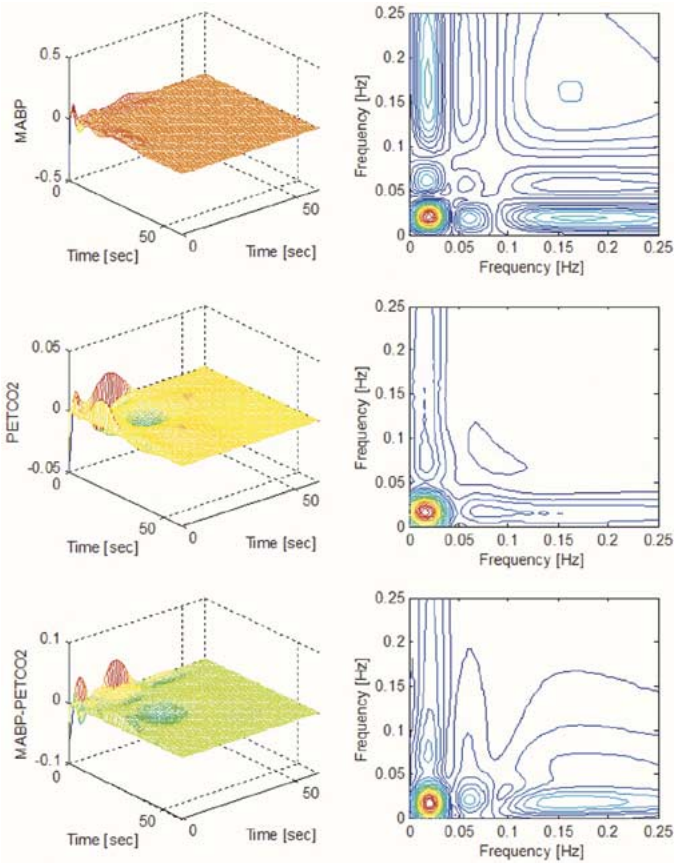

Fig. 8. Typical second-order self and cross-kernels in the time (left) and frequency (right) domains (taken from subject 091). Top: MABP kernel, middle: $P_{\mathrm{ETCO_2}}$ kernel, bottom: cross-kernel.

the $P_{\mathrm{ETCO_2}}$ frequency response a low-pass characteristic rather than the high-pass characteristic of its MABP counterpart.

Typical second-order MABP and $P_{\mathrm{ETCO_2}}$ self-kernels and the corresponding cross-kernel are shown in Fig. 8 (subject 091). Most of the power of the second-order kernels lies below 0.1 Hz. There are two diagonal peaks in the MABP second-order frequency response; a main peak at $[0.02, 0.02\ \mathrm{Hz}]$ and a secondary peak at $[0.16, 0.16\ \mathrm{Hz}]$, as well as a secondary off-diagonal peak at $[0.02, 0.16\ \mathrm{Hz}]$. The $P_{\mathrm{ETCO_2}}$ second-order frequency response has one main diagonal peak also at $[0.02, 0.02\ \mathrm{Hz}]$. The main cross-kernel peak occurs at $[0.02, 0.02\ \mathrm{Hz}]$, and a secondary one occurs at $[0.16\ \mathrm{Hz}, 0.02\ \mathrm{Hz}]$, both of them being related to the MABP and $P_{\mathrm{ETCO_2}}$ self-kernel main peaks and implying nonlinear interactions between the primary mechanisms of the two inputs acting at these specific frequency bands. Although the second-order kernels are considerably variable among different data segments, the main peak of the second-order MABP frequency response is consistent and stays within the 0.01 and 0.02 Hz bounds on the diagonal of the bi-frequency domain, while the main diagonal peak of the $P_{\mathrm{ETCO_2}}$ frequency response lies between 0 and 0.04 Hz on the diagonal (i.e., its location varies more). The cross-kernel peaks are related in general to the self-kernel peaks.

The nonstationary characteristics of the first-order MABP and $P_{\mathrm{ETCO_2}}$ kernels are tracked over the 40-min recordings by computing their fast Fourier transform (FFT) magnitude for

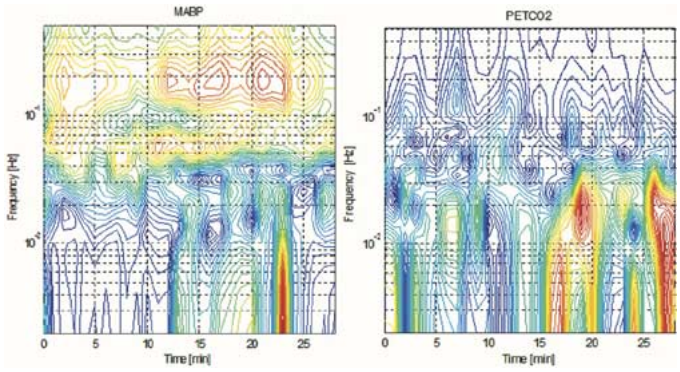

Fig. 9. The first-order frequency response functions tracked over 40 min of data (6-min sliding data segments with 5-min overlap, total of around 30 segments); subject 091. Left: MABP; right: P_{ETCO_2}.

sliding 6-min data segments with a 5-min overlap. Time-frequency contour plots of the first-order MABP and P_{ETCO_2} FFT magnitudes are shown in Fig. 9 for subject 091. The MABP frequency response exhibits nonstationarity mainly in the low-frequency range, below 0.04 Hz, and its values above that frequency (where most of its power resides) are consistent with respect to time. On the other hand, most of the power of the P_{ETCO_2} first-order frequency response resides below 0.04 Hz. The P_{ETCO_2} frequency response is also more nonstationary below 0.04 Hz and the locations of its spectral peaks vary more with respect to time than their MABP counterparts.

Following the procedure introduced in [11] to examine the nonstationarity of the second-order kernels, eigen-decomposition of the second-order MABP and P_{ETCO_2} self-kernels reveals two significant eigenvalues, which account for over 95% of the kernel power. Therefore, the corresponding eigenvectors constitute the two significant second-order modes of the system. The latter are tracked through time in the same manner as the first-order kernels and the results are shown in Fig. 10 (subject 091). While most of the MABP modes power lies below 0.05 Hz, some power resides in higher frequencies too, especially for the second mode. The latter exhibits also more spectral peaks between 0.01 and 0.1 Hz. On the other hand, most of the power of the P_{ETCO_2} modes lies below 0.02 Hz and very little power resides over 0.1 Hz. The magnitudes of the two significant eigenvalues of the MABP and P_{ETCO_2} second-order kernels are also tracked through time and the results are shown in Fig. 11 (subject 091). Considerable variability can be observed and, with the exception of the largest eigenvalue of the MABP second-order kernel, the magnitude of the eigenvalues increases with respect to time.

In order to quantify the nonstationarity of the system, a "variability index" over time for the kernel power at each discrete frequency bin f_i is computed. If $p_j(f_i)$ denotes the power at the jth data segment at f_i, defined by the FFT magnitude of the kernel, then the "variability index" can be defined as

$$I(F_i) = \frac{\left[\frac{1}{N-1}\sum_{j=1}^{N}(p_j(f_i) - p(f_i))^2\right]}{\overline{p}(f_i)} \tag{11}$$

where N is the number of segments and $\overline{p}(f_i)$ is the average of $p_j(f_i)$ over j for each frequency f_i. The computed variability indexes for the first-order kernels and second-order kernel

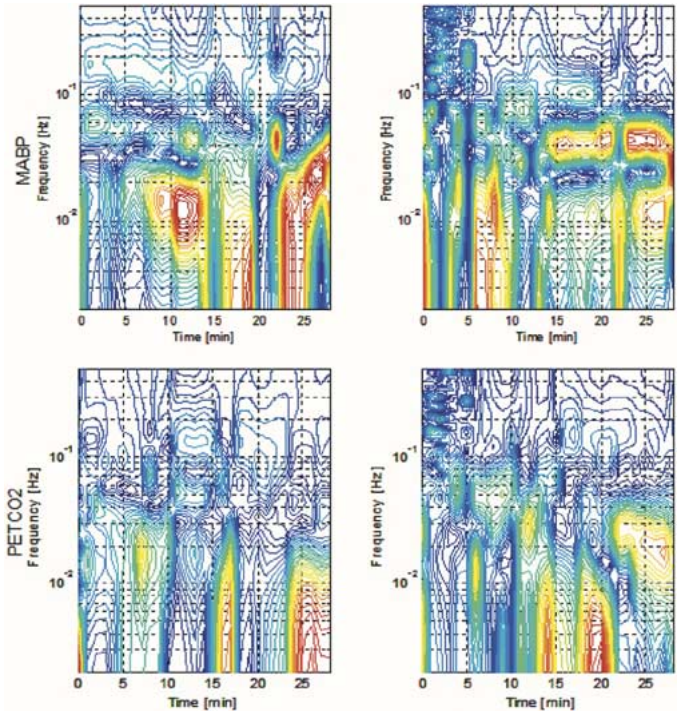

Fig. 10. Time-frequency plots of the two significant modes of the second-order kernels (top: MABP, bottom: P_{ETCO_2}), calculated from overlapping 6-min segments with a 5-min overlap (total of around 30 segments), subject 091. Left: first mode; right: second mode.

modes are shown in Fig. 12 for subject 091, both for MABP and P_{ETCO_2}. It is evident that the linear MABP dynamics are very consistent through time and that the second-order dynamics are considerably more variable [Fig. 12 (left)]. It should be also noted here that the variability of the nonlinear MABP dynamics is generally reduced when P_{ETCO_2} is used as an additional input. The variability of the first-order kernel is also reduced in the low-frequency range to a smaller extent. The P_{ETCO_2} variability indexes are shown in Fig. 12 (right). The second-order dynamics, especially the first mode dynamics, are less nonstationary than their linear counterparts above 0.1 Hz, while there are no significant differences below that frequency, where most of their power resides.

The index of (11) is computed for the obtained first and second-order dynamics over all subjects, in order to quantify their inter-subject variability. The results are shown in Fig. 13. With respect to the linear dynamics, the results agree with the observations reported above based on Fig. 6, i.e., the variability of the MABP first-order kernel is low over all frequencies, while that of its P_{ETCO_2} counterpart is higher and is slightly increased with respect to the index obtained from one subject only (Fig. 12-subject 091). On the other hand, the second-order dynamics are evidently more variable among different subjects. The computed indexes are increased for both modes of the second-order MABP and P_{ETCO_2} kernels over all frequencies, compared to the indexes computed from subject 091 (Fig. 12).

The response of the model under simulated hypercapnic or hypocapnic conditions is examined using P_{ETCO_2} long pulse stimuli in combination with shorter pulse MABP stimuli. A hypercapnic/hypocapnic pulse with a magnitude of 1 mm Hg is applied first (onset at 20 s and preserved until 420 s), followed by a pressure pulse with a magnitude of 8 mm Hg applied between

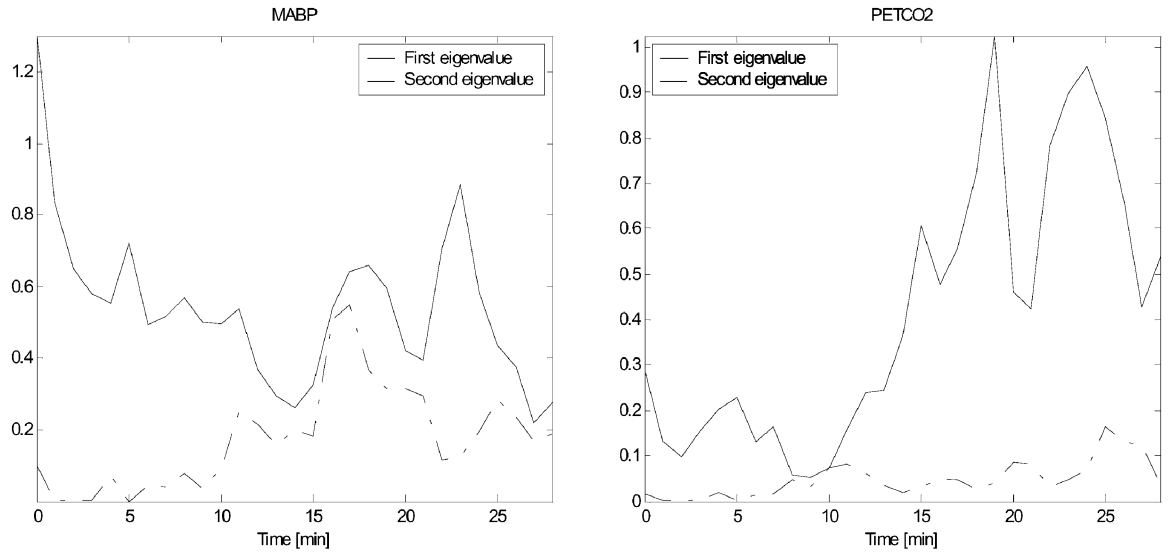

Fig. 11. Magnitude of the two significant eigenvalues of the MABP (left) and P_{ETCO_2} (right) second-order self-kernels tracked through time, subject 091. Solid line: First (largest magnitude) eigenvalue, dash-dotted line: second eigenvalue.

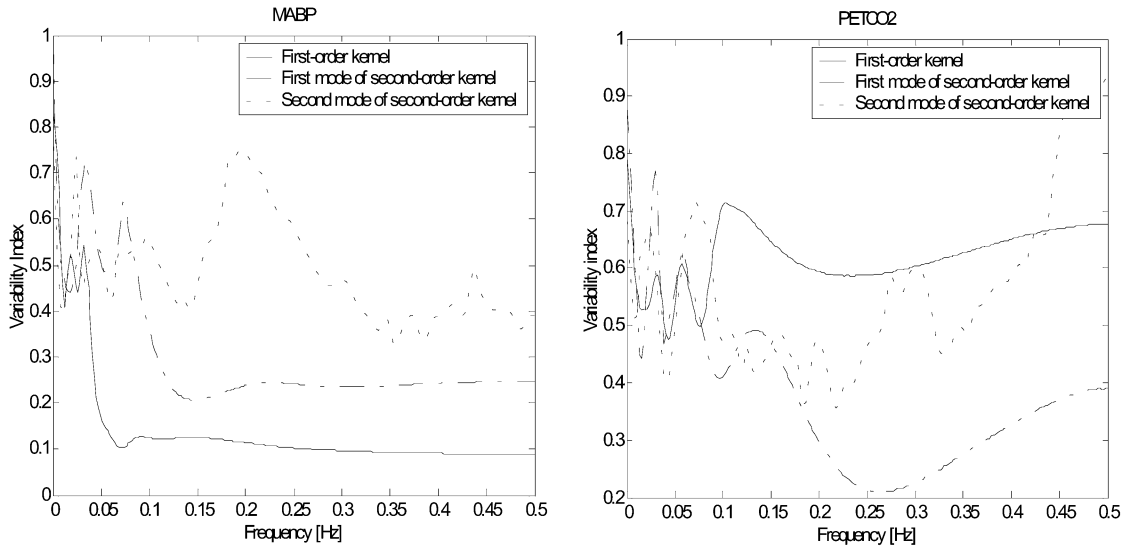

Fig. 12. Variability indexes for MABP (left) and P_{ETCO_2} (right) dynamics as a function of frequency, subject 091. Solid lines: first-order dynamics, dotted and dash-dotted lines: second-order dynamics.

150 s and 300 s. The onset/offset times are selected to allow sufficient settling time, based on the estimated kernel memories. The corresponding MCBFV responses for a typical subject/model are illustrated in Fig. 14.

The following observations can be made.

- Hypercapnia increases MCBFV and hypocapnia reduces it, as expected.
- The on-transient and off-transient responses to the MABP step are distinct in waveform (i.e., not symmetric), and the magnitude of the off-transient peak deflection is slightly larger than the corresponding on-transient peak deflection.
- The settling time of the hypercapnic on-response to the MABP step is larger (around 50 s) than that of the normocapnic or hypocapnic on-response (around 25 s).
- The settling time for the off-response transient to the MABP step is about the same (≈ 40 s) in all cases. The on and off-responses to the P_{ETCO_2} step are roughly symmetrical in waveform, although the size of the hypocapnic steady-state response is slightly larger (20%).

IV. Conclusion

Spontaneous fluctuations of MABP and MCBFV have been proven to be useful in studying the dynamic characteristics of cerebral autoregulation [6]–[11]. Based on such measurements, it has been suggested that slow pressure changes are attenuated more effectively and that significant nonlinearities are present, especially in the low-frequency range [9]–[11]. However, cerebral autoregulation is modulated by many different underlying physiological mechanisms [1]–[3]. The reactivity of cerebral vessels to CO_2 is one such mechanism, arterial CO_2 tension being an important modulator of CBFV [1]. The study of the dynamic characteristics of the P_{aCO_2}-CBFV relationship has been limited until now and was mainly based on MCBFV changes

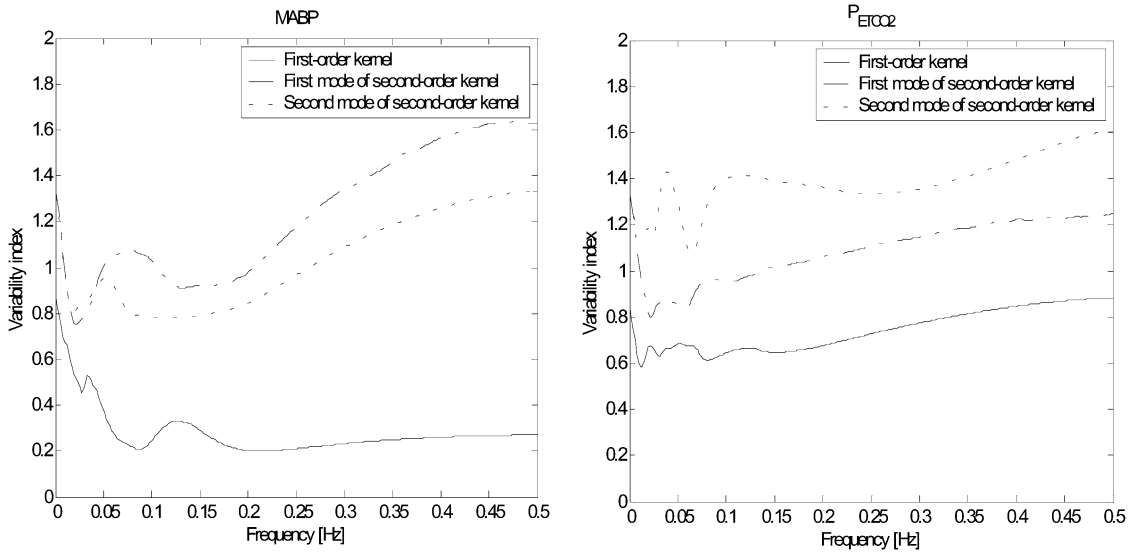

Fig. 13. Variability indexes for MABP (left) and P_{ETCO_2} (right) dynamics as a function of frequency computed over all ten subjects. Solid lines: first-order dynamics, dotted and dash-dotted lines: second-order dynamics. Note the increase in the second-order indexes compared to Fig. 12.

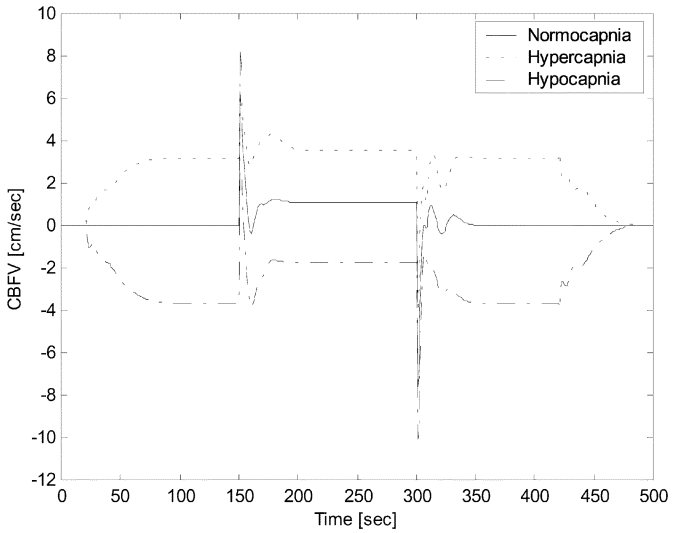

Fig. 14. Model response to MABP pulse (solid line), combined MABP pulse and hypercapnia (dotted line) and combined MABP pulse and hypocapnia (dashed-dotted line).

induced by step changes in end-tidal CO_2 [13]–[16]. However, measurements of spontaneous breath-to-breath P_{ETCO_2} fluctuations can be used to study the dynamic effect of CO_2 reactivity on autoregulation over the entire frequency range of interest, and this effect was found to be substantial [19].

In the aforementioned study, the dependence of MCBFV variations on MABP and P_{ETCO_2} fluctuations was assumed to be linear whereas it has been suggested that the MABP-MCBFV relationship exhibits significant nonlinearities [9]–[11]. Moreover, the P_{ETCO_2}-MCBFV relationship was found to be strongly nonlinear hereby, as demonstrated by the achieved prediction NMSEs when P_{ETCO_2} was used as the model input (Table II, linear NMSE: 93.2%, third-order NMSE: 71.7%); hence, the existing nonlinearities should not be neglected. It was observed that the effects of both MABP and P_{ETCO_2} are characterized by a longer memory than previously thought (MABP or P_{ETCO_2} changes occurring more than 1 min in the past affect MCBFV).

Comparison of the prediction error NMSEs achieved when either MABP or P_{ETCO_2} is used as the model input revealed that MABP explains a greater fraction of MCBFV variability, but P_{ETCO_2} explains a considerable fraction as well (prediction NMSE values of 26.8% and 71.7%, respectively, for third-order models). The contribution of the nonlinear terms was significant in both cases, but more prominent in the case of P_{ETCO_2} models. When both MABP and P_{ETCO_2} were used as inputs, a reduction of around 6% in the achieved prediction NMSE was observed, compared to MABP models, with the output prediction NMSE reduction due to the nonlinear model terms being equal to 18%. Note that second-order models appear from the observations to perform better when modeling the MABP-MCBFV relationship in terms of prediction NMSE, as reported also in [11], but third-order models appear to perform better when P_{ETCO_2} fluctuations are incorporated, implying a higher order effect of P_{ETCO_2} on MCBFV. Decomposition of the model output terms into pressure and CO_2 terms revealed that the former account for around 60% of the total output power, while the latter account for around 20%. The remaining 20% corresponds to the nonlinear interaction terms between them, indicating a significant contribution of the interaction terms, contrary to what was reported in [19] (Table III—average NMSE reduction due to cross-terms is over 27%).

The spectral content of the first-order and total (i.e., second- and third-order) residuals revealed that nonlinearities are active in the low-frequency range (below 0.04 Hz), agreeing with [11]. By examining the residuals of the pressure terms, it was observed that MABP terms act mainly above 0.04 Hz, whereas CO_2 and nonlinear interaction terms act mainly below 0.04 Hz. This implies that the effects of MABP on MCBFV are mostly linear (though there is a nonlinear component as well), while the effects of CO_2 are strongly nonlinear. More than 50% of the CO_2 contribution power is accounted for by the corresponding

(self) nonlinear terms, as indicated by the corresponding mean power ratio of nonlinear-to-linear output components, which is equal to 1.18 (Table IV).

The linear MABP dynamics (first-order kernels) exhibit a differentiating (high-pass) characteristic. Their form is not affected by the inclusion of $P_{\mathrm{ETCO_2}}$ variations in the model, compared to results obtained hereby and in previously reported studies [11], except for a decrease in the MABP kernel power in the low-frequency range. This is related to the fact that CO_2 acts mainly in the low frequencies. The negative undershoot observed after the initial large value is indicative of an autoregulatory response and the high-pass characteristic implies that slow MABP changes are regulated more effectively. The first-order $P_{\mathrm{ETCO_2}}$ kernels exhibit slower dynamics and an integrating (low-pass) characteristic. The presence of a pure time delay on the order of 3–4 s in the action of CO_2 was associated to the high variance observed for the (linear and nonlinear) kernel values in the initial time lags. This agrees with the results reported in [16], whereby a delay of 3.9 s was estimated based on the MCBFV responses to hypocapnic $P_{\mathrm{ETCO_2}}$ stimuli. The form of the first-order MABP kernels was consistent among different subjects (Figs. 6 and 13), while their $P_{\mathrm{ETCO_2}}$ counterparts exhibited more variability (Figs. 7 and 13), a fact that was also reported in [19] for the corresponding impulse responses. Regarding the second-order kernels, it was found that most of their power lies below $[0.04\ \mathrm{Hz}, 0.04\ \mathrm{Hz}]$ in the bi-frequency domain and that they exhibit more variability among different subjects than their first-order counterparts (Fig. 13).

The time-varying characteristics of cerebral autoregulation were studied by tracking the first- and second-order frequency responses (for both MABP and $P_{\mathrm{ETCO_2}}$) for sliding 6-min data segments with a 5-min overlap. Significant nonstationarities of no apparent pattern were observed, as demonstrated also in [11] for the dynamics of the MABP-MCBFV relationship. The second-order dynamics were found to be more variable with respect to time than their linear counterparts for MABP but not for $P_{\mathrm{ETCO_2}}$, as shown in Fig. 12. Therefore, whereas for $P_{\mathrm{ETCO_2}}$ the second-order dynamics appear to be less nonstationary but more variable with respect to different subjects, the MABP second-order dynamics appear to be both more nonstationary and variable among different subjects. The nonstationarity of the system, especially that observed for the nonlinear dynamics, is reflected on the achieved out-of-sample prediction NMSE. The average value of the latter over all subjects is equal to $74.7 \pm 13.5\%$, while the linear component of the model achieves an average out-of-sample NMSE of $64.4 \pm 14.2\%$, i.e., in most cases the nonlinear terms do not improve the out-of-sample NMSE because of their fast-changing characteristics. The out-of-sample prediction NMSE follows roughly a χ^2 distribution, its values ranging from as low as 20% (i.e., comparable to in-sample NMSE) to as high as over 100%.

The form of the responses to MABP and $P_{\mathrm{ETCO_2}}$ step changes demonstrated the autoregulatory characteristics of the obtained models in a quantitative manner, but exhibit some differences compared to previously reported results [15], [16], where the CBFV responses to step increases in $P_{\mathrm{ETCO_2}}$ were found to be much slower than the responses to step decreases in $P_{\mathrm{ETCO_2}}$. This may be due to the fact that our model was estimated based on small fluctuations of $P_{\mathrm{ETCO_2}}$ around its mean value, whereas in [15] and [16] large changes in $P_{\mathrm{ETCO_2}}$ were induced.

The effect of the two major physiological signals modulating CBF regulation, namely MABP and $P_{\mathrm{ETCO_2}}$, were assessed in a multiple-input and nonlinear context. The results of this study indicate the usefulness of the proposed methodology in modeling nonlinear multiple-input systems and in quantifying the linear and nonlinear effects of MABP and $P_{\mathrm{ETCO_2}}$ on MCBFV as well as the effect of their nonlinear interactions. The same can be done for other exogenous variables affecting autoregulation and may lead to a better understanding of the underlying physiological mechanisms under normal and pathophysiological conditions.

REFERENCES

[1] D. D. Heistad and H. A. Kontos, "Cerebral circulation," in *Handbook of Physiology. The Cardiovascular System. Peripheral Circulation and Organ Blood Flow*. Bethesda, MD: Amer. Physiol. Soc., 1983, pt. 1, vol. III, ch. 5, sec. 2, pp. 137–182.

[2] O. B. Paulson, B. Strandgaard, and L. Edvinsson, "Cerebral autoregulation," *Cerebrovasc. Brain Metab. Rev.*, vol. 2, pp. 161–192, 1990.

[3] L. Edvinsson and D. N. Krause, *Cerebral Blood Flow and Metabolism*. Philadelphia, PA: Lippincott Williams and Wilkins, 2002.

[4] D. J. Marsh, J. L. Osborn, and W. J. Cowley, "1/f fluctuations in arterial pressure and regulation of renal blood flow in dogs," *Amer. J. Physiol. 258 (Renal Fluid Electrolyte Physiol. 27)*, pp. F1394–1400, 1990.

[5] R. Zhang, J. H. Zuckerman, and B. D. Levine, "Spontaneous fluctuations in cerebral blood flow velocity: Insights from extended duration recordings in humans," *Amer. J. Physiol. 278 (Heart Circ. Physiol.)*, pp. H1848–1855, 2000.

[6] C. A. Giller, "The frequency-dependent behavior of cerebral autoregulation," *Neurosurgery*, vol. 27, pp. 362–368, 1990.

[7] T. B. J. Kuo, C. M. Chern, W. Y. Sheng, W. J. Wong, and H. H. Hu, "Frequency domain analysis of cerebral blood flow velocity and its correlation with arterial blood pressure," *J. Cereb. Blood Flow Metab.*, vol. 18, pp. 311–318, 1998.

[8] R. B. Panerai, A. W. R. Kelsall, J. M. Rennie, and D. H. Evans, "Frequency-domain analysis of cerebral autoregulation from spontaneous fluctuations in arterial blood pressure," *Med. Biol. Eng. Comput.*, vol. 36, pp. 315–322, 1998.

[9] R. Zhang, J. H. Zuckerman, C. A. Giller, and B. D. Levine, "Transfer function analysis of dynamic cerebral autoregulation in humans," *Amer. J. Physiol. 274 (Heart Circ. Physiol. 43)*, pp. H233–H241, 1998.

[10] R. B. Panerai, S. L. Dawson, and J. F. Potter, "Linear and nonlinear analysis of human dynamic cerebral autoregulation," *Amer. J. Physiol. 277 (Heart Circ. Physiol. 46)*, pp. H1089–H1099, 1999.

[11] G. D. Mitsis, R. Zhang, B. D. Levine, and V. Z. Marmarelis, "Modeling of nonlinear systems with fast and slow dynamics. II. Application to cerebral autoregulation in humans," *Ann. Biomed. Eng.*, vol. 30, pp. 555–565, 2002.

[12] F. Gotoh, Y. Tazaki, and J. S. Meyer, "Transport of blood gases through brain and their extravascular vasomotor system," *Exp. Neurol.*, vol. 4, pp. 48–58, 1961.

[13] D. A. Wilson, R. J. Traystman, and C. E. Rapela, "Transient analysis of the canine cerebrovascular response to carbon dioxide," *Circ. Res.*, vol. 56, pp. 596–605, 1985.

[14] I. Ellingsen, A. Hauge, G. Nicolaysen, M. Thoresen, and L. Walloe, "Changes in human cerebral blood flow due to step changes in $P_{\mathrm{AO_2}}$ and $P_{\mathrm{ACO_2}}$," *Acta Physiol. Scand.*, vol. 129, pp. 157–163, 1987.

[15] M. J. Poulin, P.-J. Liang, and P. A. Robbins, "Dynamics of the cerebral blood flow response to step changes in end-tidal $P_{\mathrm{CO_2}}$ and $P_{\mathrm{O_2}}$ in humans," *J. Appl. Physiol.*, vol. 81, pp. 1084–1095, 1996.

[16] ——, "Fast and slow components of cerebral blood flow response to step decreases in end-tidal $P_{\mathrm{CO_2}}$ in humans," *J. Appl. Physiol.*, vol. 85, no. 2, pp. 388–397, 1998.

[17] M. Ursino and C. A. Lodi, "Interaction among autoregulation, CO_2 reactivity and intracranial pressure: A mathematical model," *Amer. J. Physiol.*, vol. 274, pp. H1715–H1728, 1998.

[18] M. Ursino, A. Ter Minassian, C. A. Lodi, and L. Beydon, "Cerebral hemodynamics during arterial and CO_2 pressure changes: *In vivo* prediction by a mathematical model," *Amer. J. Physiol.*, vol. 279, pp. H2439–H2455, 2000.

[19] R. B. Panerai, D. M. Simpson, S. T. Deverson, P. Mahony, P. Hayes, and D. H. Evans, "Multivariate dynamic analysis of cerebral blood flow regulation in humans," *IEEE Trans. Biomed. Eng.*, vol. 47, pp. 419–421, Mar. 2000.

[20] G. D. Mitsis and V. Z. Marmarelis, "Modeling of nonlinear systems with fast and slow dynamics. I. Methodology," *Ann. Biomed. Eng.*, vol. 30, pp. 272–281, 2002.

[21] G. D. Swanson and J. W. Belville, "Step changes in end tidal CO_2: Methods and implications," *J. Appl. Physiol.*, vol. 39, pp. 377–385, 1975.

[22] P. A. Robbins, G. D. Swanson, and M. G. Howson, "A prediction correction scheme for forcing alveolar gases along certain time courses," *J. Appl. Physiol.*, vol. 52, pp. 1353–1357, 1982.

[23] P. A. Robbins, J. Conway, D. A. Cunningham, S. Khamnei, and D. J. Patterson, "A comparison of indirect methods for continuous estimation of arterial P_{CO_2} in men," *J. Appl. Physiol.*, vol. 68, pp. 1727–1731, 1990.

[24] J. S. Williams and T. G. Babb, "Differences between estimates and measured P_{aCO_2} during rest and exercise in older subjects," *J. Appl. Physiol.*, vol. 83, pp. 312–316, 1997.

[25] B. P. Imholz, J. J. Settels, A. H. van der Meiraker, K. H. Wesseling, and W. Wieling, "Non-invasive continuous finger blood pressure measurement during orthostatic stress compared to intra-arterial pressure," *Cardiovasc. Res.*, vol. 24, pp. 214–221, 1990.

[26] S. Omboni, G. Parati, A. Frattola, E. Mutti, M. Di Rienzo, P. Catiglioni, and G. Mancia, "Spectral and sequence analysis of finger blood pressure variability: Comparison with analysis of intra-arterial recordings," *Hypertension*, vol. 22, pp. 26–33, 1993.

[27] R. Aaslid, T. Markwalder, and H. Normes, "Noninvasive transcranial Doppler ultrasound recording of flow velocity in basal cerebral arteries," *J. Neurosurg.*, vol. 57, pp. 769–774, 1982.

[28] M. J. Poulin and P. A. Robbins, "Indexes of flow and cross-sectional area in the middle cerebral artery using Doppler ultrasound during hypoxia and hypercapnia in humans," *Stroke*, vol. 27, pp. 2244–2250, 1996.

[29] P. Z. Marmarelis and V. Z. Marmarelis, *Analysis of Physiological Systems: The White Noise Approach* New York, Plenum, 1978.

[30] V. Z. Marmarelis, "Modeling methodology for nonlinear physiological systems," *Ann. Biomed. Eng.*, vol. 25, pp. 239–251, 1997.

[31] G. D. Mitsis and V. Z. Marmarelis, "Nonlinear modeling of physiological systems with multiple inputs," in *Proc. 2nd Joint Meet. IEEE EMBS/BMES*, vol. 1, Houston, TX, 2002, pp. 21–22.

[32] J. Rissanen, "Information theory and neural nets," in *Mathematical Perspectives on Neural Networks*, P. Smolensky, M. C. Mozer, and D. E. Rumelhart, Eds. Mahwah, NJ: Lawrence Erlbaum Associates, 1996, pp. 567–602.

Georgios D. Mitsis (S'99–M'02) was born in Ioannina, Greece, on February 5, 1975. He received the Diploma in electrical and computer engineering from the National Technical University of Athens, Athens, Greece, in 1997, the M.S. degree in biomedical engineering, the M.S. degree in electrical engineering and the Ph.D. degree in biomedical engineering from the University of Southern California, Los Angeles, CA, in 2000, 2001, and 2002, respectively.

He is currently a postdoctoral Research Associate at the Biomedical Simulations Resource Research Center of the University of Southern California, Los Angeles. His research interests include biomedical signal processing and identification and modeling of nonlinear and time-varying systems, with applications to physiological systems. In this context, he is particularly interested in dynamic cerebral autoregulation under normal and pathophysiological conditions. He is also interested in bioelectromagnetism.

Dr. Mitsis is a member of the Biomedical Engineering Society (BMES) and of the Technical Chamber of Greece.

Marc J. Poulin was born in Timmins, ON, Canada, on March 21, 1963. He received the B.S. degree in physical and health education from Laurentian University, Sudbury, ON, Canada, in 1986, M.A. and Ph.D. degrees in kinesiology (cardiorespiratory physiology and ageing) from the University of Western Ontario, London, ON, Canada, in 1988 and 1993, and a D.Phil. degree in physiological sciences (human physiology) from the University of Oxford, Oxford, U.K., in 1999.

He carried out postdoctoral work with Prof. P. A. Robbins at the University Laboratory of Physiology in Oxford (1993–2000). In 2000, he joined the Faculties of Medicine (Departments of Physiology and Biophysics and Clinical Neurosciences) and Kinesiology at the University of Calgary, Calgary, AB, Canada, where he is now Associate Professor. He is a New Investigator with the Canadian Institutes of Health Research (CIHR) and a Medical Scholar with the Alberta Heritage Foundation for Medical Research (2000–2005). His research is funded by grants from the CIHR, the Heart and Stroke Foundation of Alberta, NWT and Nunavut, and the Canadian Foundation for Innovation. His main research interests include the mechanisms by which oxygen and carbon dioxide regulate cerebral blood flow in young humans, how these mechanisms become altered with advancing age, with diseases such as obstructive sleep apnea, and with acclimatization to the hypoxia of altitude.

Peter A. Robbins was born in Bristol, U.K., on August 28, 1957. He studied at Keble College, Oxford, U.K. where he received a first-class honors degree in physiology in 1978, the D.Phil. degree in physiology in 1981 for which he was awarded the Gotch Prize, and the B.M. and B.Ch. degrees in clinical medicine in 1984. He received a first-class honors degree in mathematics from the Open University in 1992.

After completing his preregistration training in medicine in 1985, he took a staff position as a University Lecturer in Physiology at Oxford University, Oxford, U.K., in 1985 together with a Fellowship and Praelectorship at the Queen's College, Oxford. He has been Professor of Physiology since 1998, and has served both as Head of Department and as Chairman of the Faculty. The main focus of his research activity has been understanding the nature of the algorithms that underlie cardiorespiratory control, in particular the regulation of breathing and of vascular tone. His particular areas of interest within this theme have included the roles of hypoxia and carbon dioxide in the regulatory process and the mechanisms by which homeostasis is maintained during exercise.

Vasilis Z. Marmarelis (M'79–SM'94–F'97) was born in Mytilini, Greece, on November 16, 1949. He received the Diploma degree in electrical and mechanical engineering from the National Technical University of Athens, Athens, Greece, in 1972 and the M.S. and Ph.D. degrees in engineering science (information science and bioinformation systems) from the California Institute of Technology, Pasadena, in 1973 and 1976, respectively.

After two years of postdoctoral work at the California Institute of Technology, he joined the faculty of Biomedical and Electrical Engineering at the University of Southern California, Los Angeles, where he is currently Professor and Director of the Biomedical Simulations Resource, a research center funded by the National Institutes of Health since 1985 and dedicated to modeling/simulation studies of biomedical systems. He served as Chairman of the Biomedical Engineering Department from 1990 to 1996. His main research interests are in the areas of nonlinear and nonstationary system identification and modeling, with applications to biology, medicine, and engineering systems. Other interests include spatiotemporal and nonlinear/nonstationary signal processing, and analysis of neural systems and networks with regard to information processing. He is coauthor of the book *Analysis of Physiological Systems: The White-Noise Approach* (New York: Plenum, 1978; Russian translation: Moscow, Mir Press, 1981; Chinese translation: Academy of Sciences Press, Beijing, 1990) and editor of three volumes on *Advanced Methods of Physiological System Modeling* (1987, 1989, and 1994). He has published more than 100 papers and book chapters in the area of system and signal analysis. His most recent book, is"Nonlinear Dynamic Modeling of Physiological Systems," (Piscataway, NJ: Wiley/IEEE, 2004).